

# Chemical Sensing Systems that Utilize Soft Electronics on Thin Elastomeric Substrates with Open Cellular Designs

Yoon Kyeong Lee, Kyung-In Jang, Yinji Ma, Ahyeon Koh, Hang Chen, Han Na Jung, Yerim Kim, Jean Won Kwak, Liang Wang, Yeguang Xue, Yiyuan Yang, Wenlong Tian, Yu Jiang, Yihui Zhang, Xue Feng, Yonggang Huang, and John A. Rogers\*

A collection of materials and device architectures are introduced for thin, stretchable arrays of ion sensors that mount on open cellular substrates to facilitate solution exchange for use in biointegrated electronics. The results include integration strategies and studies of fundamental characteristics in chemical sensing and mechanical response. The latter involves experimental measurements and theoretical simulations that establish important considerations in the design of low modulus, stretchable properties in cellular substrates, and in the realization of advanced capabilities in spatiotemporal mapping of chemicals' gradients. As the chemical composition of extracellular fluids contains valuable information related to biological function, the concepts introduced here have potential utility across a range of skin- and internal-organ-integrated electronics where soft mechanics, fluidic permeability, and advanced chemical sensing capabilities are key requirements.

## 1. Introduction

Recent advances in flexible and stretchable electronics establish the foundations for advanced physiological recording systems that mount on the curvilinear surfaces of nearly any region of the body, on nearly any organ system.<sup>[1–9]</sup> Due to the intrinsically low elastic moduli and bending stiffnesses of the biocompatible materials used in these platforms, the devices can intimately integrate with soft biological tissues for continuous collection of healthcare-related data without mechanically induced irritation, discomfort, or interfacial degradation.<sup>[7–12]</sup> Although capabilities in conformal and

Y. K. Lee

Department of Chemistry  
University of Illinois at Urbana–Champaign  
Urbana, IL 61801, USA

Y. K. Lee, Prof. K.-I. Jang, H. N. Jung, Y. Kim, J. W. Kwak, Y. Yang  
Department of Materials Science and Engineering  
Frederick Seitz Materials Research Laboratory  
University of Illinois at Urbana–Champaign  
Urbana, IL 61801, USA

Prof. K.-I. Jang  
Department of Robotics Engineering  
Daegu Gyeongbuk Institute of Science and Technology (DGIST)  
Daegu 42988, South Korea

Dr. Y. Ma, Dr. H. Chen, Dr. L. Wang, Y. Xue, W. Tian, Y. Jiang,  
Prof. Y. Zhang, Prof. Y. Huang  
Department of Civil and Environmental Engineering  
Mechanical Engineering  
Materials Science and Engineering  
Northwestern University  
Evanston, IL 60208, USA

Dr. Y. Ma, Dr. H. Chen, Prof. Y. Zhang, Prof. X. Feng  
Department of Engineering Mechanics, Center for  
Mechanics and Materials  
Tsinghua University  
Beijing 100084, China

Prof. A. Koh  
Department of Biomedical Engineering  
Binghamton University  
4400 Vestal Parkway East, Binghamton, NY 13902, USA

DOI: 10.1002/adfm.201605476

Dr. L. Wang

Institute of Chemical Machinery and  
Process Equipment  
Department of Chemical and Biological Engineering  
Zhejiang University  
Hangzhou 310027, China

W. Tian  
School of Mechanical Engineering  
Northwestern Polytechnical University  
Xi'an 710072, China

Y. Jiang  
Institute of Semiconductors  
Chinese Academy of Sciences  
Beijing 100083, China

Prof. J. A. Rogers  
Center for Bio-Integrated Electronics  
Departments of Materials Science and Engineering  
Biomedical Engineering, Chemistry Mechanical Engineering  
Electrical Engineering and Computer Science  
Neurological Surgery  
Simpson Querrey Institute for BioNanotechnology  
McCormick School of Engineering and Feinberg School of Medicine  
Northwestern University  
Evanston, IL 60208, USA  
E-mail: jrogers@northwestern.edu



robust contact are well established through prior studies, materials and designs that minimize or eliminate disruptions to natural diffusive or convective flow of fluids through the device are less well explored.<sup>[13,14]</sup> These types of device-induced fluid perturbations can represent critical disadvantages in sensing of chemical biomarkers such as glucose and ions since stagnation of fluid can cause artificial accumulation or depletion of chemicals of interest. Open, cellular designs in substrates for soft electronics can consist of a combination of porous and planar areas for fluid transport and device support, respectively. Such an architecture allows fluid diffusion across a low modulus elastomer membrane while maintaining robust mounting locations for sensors and their interconnects. Although these options offer many attractive features, the integration of electrodes and electronics on such substrates involves challenges in fabrication and assembly.

This paper presents materials, designs, and integration strategies for thin, stretchable ion sensors that mount on cellular substrates with well-defined geometries. By comparison to previously reported wearable ion sensors,<sup>[15,28]</sup> our systems are different in their use of multiplexed arrays of sensors for spatial mapping of ion concentration and elastomeric cellular substrates for improved mechanics and permeability. Specifically, the configuration involves sensing arrays surrounded by porous areas that facilitate diffusive, convective, and actively forced flows of biofluids. This heterogeneous design layout provides key advantages over conventional alternatives in both its stretchable mechanics and in the unconstrained hydrodynamics of the surrounding biofluids. Systematic studies of the mechanical properties show improved elastic responses and reduced moduli, both of which substantially reduce mechanical loads on the targeted biological surfaces. A biofluid permeable interface enables accurate spatiotemporal mapping of ion concentrations. Because the composition of extracellular fluid such as sweat and interstitial fluid contains valuable information related to biological processes,<sup>[15,16,28]</sup> this combination of chemical sensing capabilities with stretchable cellular substrates offers potential for use across a diverse set of skin and other organ-integrated electronics systems.

## 2. Results and Discussion

Figure 1a presents a schematic diagram of an array of chemical sensors on an elastomeric cellular substrate. Each device incorporates an ion selective membrane based on poly(vinyl chloride) (PVC) (gray in Figure 1a) coated on a layer of electrodeposited poly(3,4-ethylenedioxythiophene)/polystyrene sulfonate (PEDOT/PSS) conducting polymer (black).<sup>[17]</sup> The ion selectivity results from ionophores embedded in the PVC membrane that selectively binds to targeted ions.<sup>[18]</sup> This binding leads to an electrical potential across the membrane/solution interface, thus serving as a potentiometric sensing interface for ions present in the surrounding fluid. Interconnecting wires (Au, light yellow) adopt a lithographically defined serpentine design to allow biaxial stretchability, and connect to bonding pads that support wiring to an external potentiostat. Figure 1b shows a representative thin, flexible ion sensor mounted on a

stretchable cellular substrate of poly(dimethylsiloxane) (PDMS), dyed black to enhance visibility.

The sequence of fabrication steps is summarized in Figure 1c,d. As described in the Experimental Section, the array of ion sensors consists of eight 0.5 mm<sup>2</sup> electrodes with total thicknesses of  $\approx 50$   $\mu\text{m}$  (5 nm Cr/200 nm Au/150 nm PEDOT/50  $\mu\text{m}$  PVC-based membrane). Fabrication began with photolithographic patterning of metals deposited by electron beam evaporation on a polyimide (PI) film. An additional layer of PI served to encapsulate the Au metal layers except for locations of openings that define the sensing interface. Immersing the sample into acetone removed a sacrificial layer of poly(methyl methacrylate) (PMMA, 1  $\mu\text{m}$ ) beneath the PI film, to allow retrieval of the sensor electrode arrays onto a water-soluble tape. Electron beam evaporation formed a thin film of SiO<sub>2</sub> (50 nm) to allow siloxane bonding between the sensor arrays and the PDMS substrate.

In a separate set of steps, fabrication of the cellular substrate started with spin coating of a PDMS polymer on a mold formed by photolithographic patterning of a thick (300  $\mu\text{m}$ ) layer of a photocurable epoxy material (SU-8). Thermally curing the PDMS and delaminating it from the mold formed a cellular substrate in the inverse geometry of the mold. Exposing the surface of the PDMS substrate to ultraviolet/ozone yielded exposed hydroxyl groups to facilitate formation of siloxane bonds. Transferring the sensor array with careful registration led to strong mechanical adhesion based on this chemistry. Dissolving the water-soluble tape completed the fabrication.

The steps for preparing the ion selective electrodes are described in Figure 1d. The scanning electron microscopy image in Figure 1d shows a magnified view of a single Au electrode before electrodeposition of PEDOT/PSS to form a conductive polymer layer.<sup>[17]</sup> This process involved 15 cycles of cyclic voltammetry (CV, from  $-0.2$  to  $1$  V,  $20$  mV s<sup>-1</sup>) to yield smooth, crack-free, and well-adhered films. The black center area in the inset of Figure 1d corresponds to the PEDOT/PSS. Drop casting PVC dissolved in tetrahydrofuran (THF) yielded ion selective membranes on top of the conductive polymer. Surface tension and the viscosity of the membrane cocktail prevented spreading beyond the areas defined by the PI encapsulation layer. Figure 1e,f outlines the vertical structure of the ion selective electrode with membrane coating and the details of a serpentine interconnect suspended above an opening in the cellular substrate.

Figure 1g demonstrates the essential permeability of water across the cellular substrate in a setup that involves a sensor fixed on agarose gel and immersed in a water bath. A thin tube embedded in the agarose allowed controlled introduction of water dyed blue for ease of visualization. The picture shows diffusion of this infused water through the pores in the substrate. Finite element analysis (FEA, FLUENT commercial software,<sup>[19]</sup> ANSYS) captures the diffusion of ion-containing water (with injection velocity of  $10$  mm s<sup>-1</sup> and concentration of  $1$  M) injected into a closed chamber filled with free water (with the geometric parameters given in Figure S1 in the Supporting Information) for  $1$  s, for cases with and without the cellular substrate. The diffusivity of the ions is  $2 \times 10^{-9}$  m<sup>2</sup> s<sup>-1</sup>, the value for K<sup>+</sup> in water at room temperature.<sup>[20]</sup> The simulated time sequence of ion diffusion with the cellular substrate (Figure 1h)

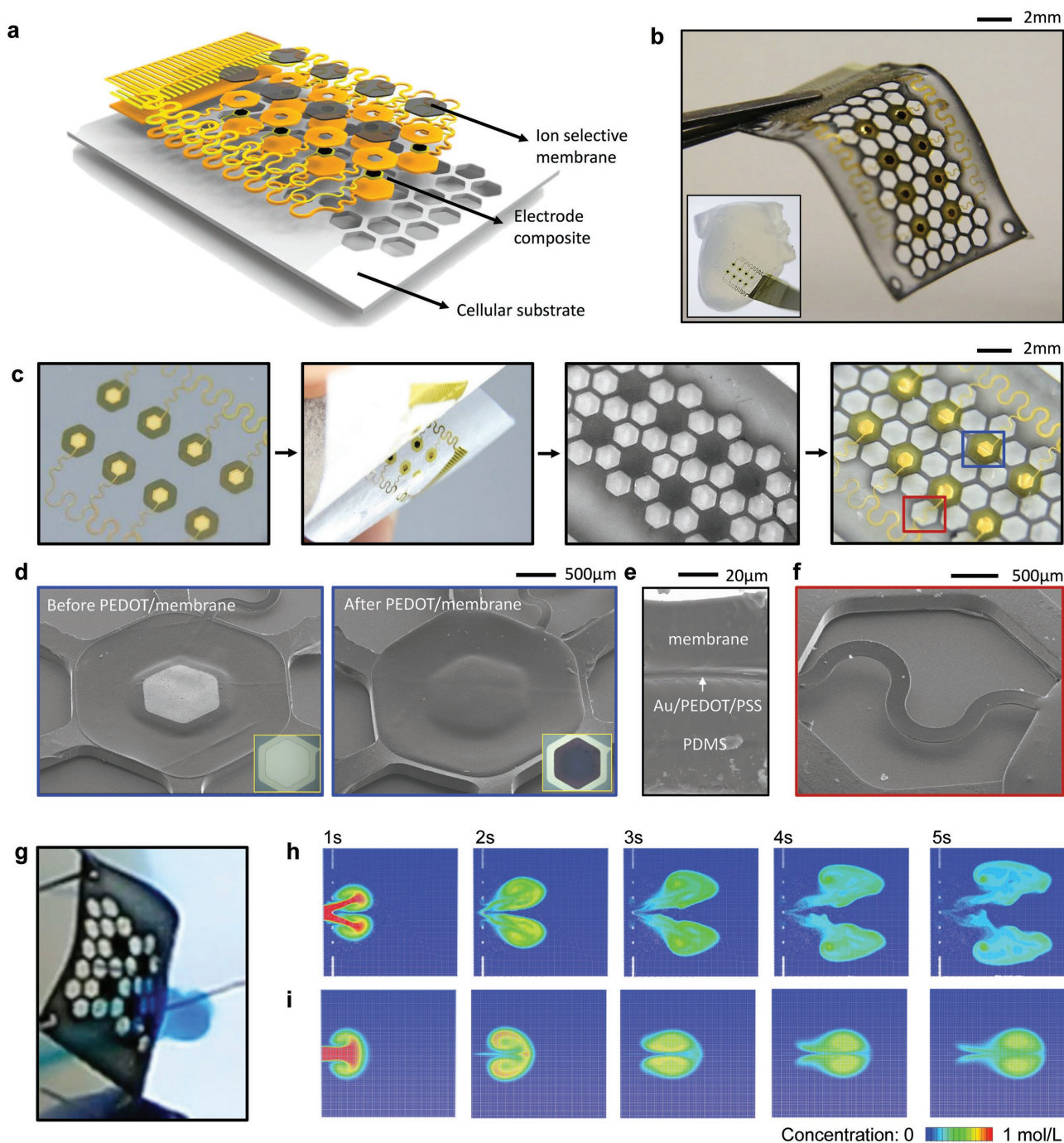


**Figure 1.** Thin, stretchable array of ion selective sensors on a cellular substrate: a) Schematic diagram of the sensor design. b) Optical image of the fabricated ion sensor on a cellular substrate. b, inset) Ion sensor mounted on a rabbit heart model constructed from agarose gel. c, d) Fabrication procedure: c) optical images of microfabrication procedure before PEDOT/PSS and ion selective membrane coating; d) scanning electron microscopy (SEM) images of the electrode before and after PEDOT/PSS and ion selective membrane coating; d, insets) optical image of the electrode before and after PEDOT/PSS electrodeposition without membrane coating. e) Cross-sectional view of the ion selective electrode with membrane coating. f) Serpentine interconnect suspended above an opening in the cellular substrate. g) Water permeation test through a cellular substrate. Injected water is dyed blue for visualization. h, i) Simulated time sequence of ion diffusion with (h) and without (i) cellular substrate.

indicates similar levels of diffusion as those without the substrate (Figure 1i).

Figure 2 highlights the stretchable mechanics associated with the cellular design. The porosity of the substrate can

be expressed as  $\Phi = (1 - \delta/d)^2$ , where  $d$  and  $\delta$  represent the spacing of the cells and the thickness of cellular wall, respectively. (Figure S2, Supporting Information). As in Figure 2a, the stress-strain curves obtained by FEA (ABAQUS commercial

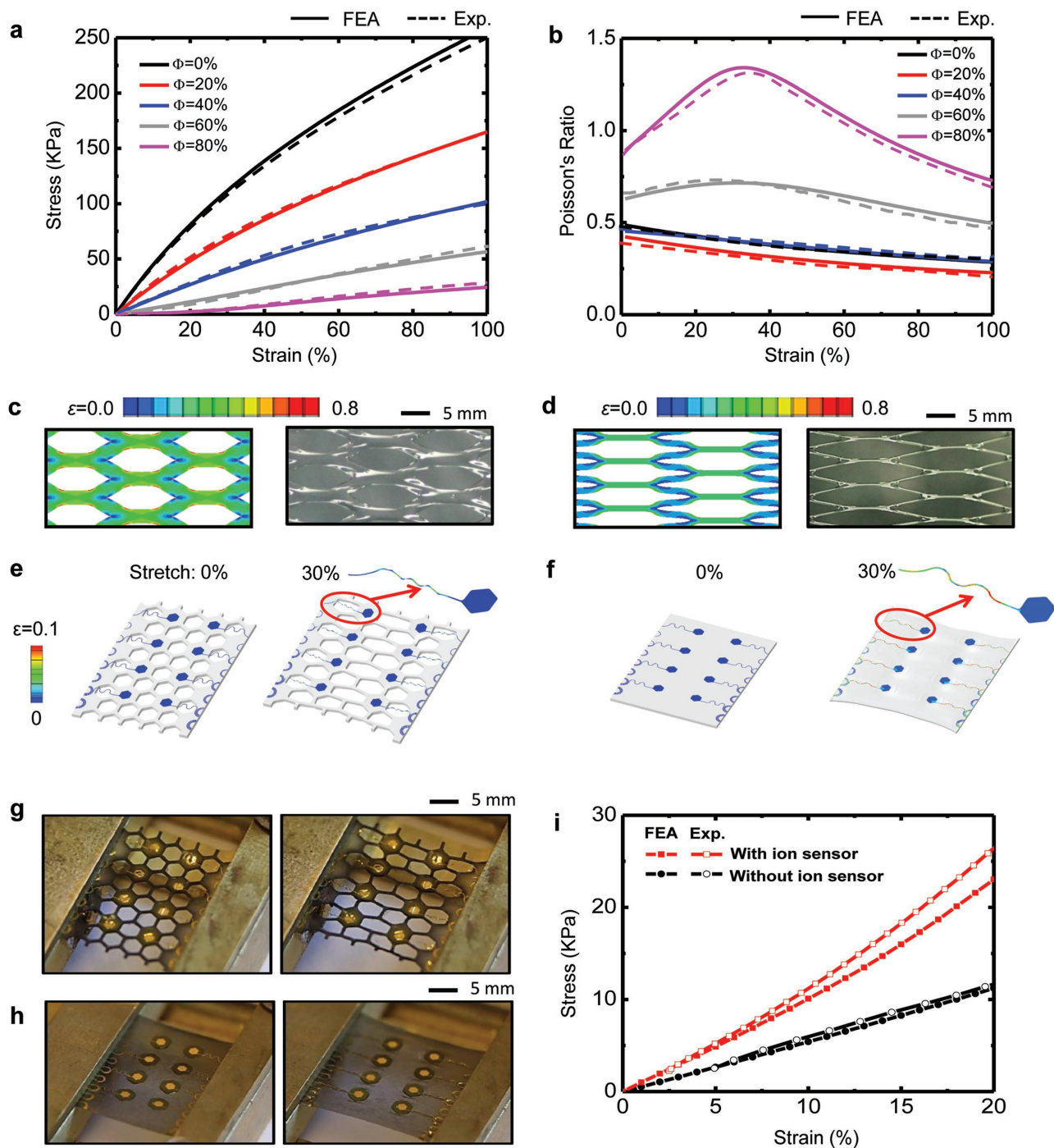


**Figure 2.** Mechanics of cellular substrates: a,b) Stress–strain curves (a) and Poisson’s ratios (b) at different porosities. c,d) Numerical results (left) and optical images (right) of the cellular substrates at low (40%) (c) and high (80%) (d) porosity under 60% stretching. e,f) Numerical results of the cellular (e) and solid (f) substrates with the ion sensor under 30% stretching. g,h) Optical images of cellular (g) and solid (h) substrates with ion sensors under 30% stretching. i) Stress–strain curves of a cellular substrate with and without sensors.

software,<sup>[21]</sup> ABAQUS Inc.) for the cellular substrate (PDMS with modulus of 0.5 MPa and Poisson’s ratio of 0.5) at different porosities ( $\Phi = 0, 20\%, 40\%, 60\%$ , and  $80\%$ ) agree well with the experiments, without any parameter fitting. The effective modulus decreases monotonically as the porosity increases. The stress–strain curve displays a “J shape” at high porosity

$\Phi = 80\%$  (Figure 2a; and also Figure S3c, Supporting Information for a magnified view) and  $\Phi = 95\%$  (Figure S3d, Supporting Information), but not at low and medium porosities ( $\Phi \leq 60\%$ ; Figure S3a and b, Supporting Information). In addition, the Poisson’s ratio ( $\nu = -\epsilon_{yy}/\epsilon_{xx}$ , where  $\epsilon_{yy}$  is the lateral strain under  $\epsilon_{xx}$  stretching) increases quickly with  $\Phi$  at high

porosity, but becomes insensitive to  $\Phi$  at low porosity (Figure 2b). These different behaviors at high and low porosities result from the effect of bending, as illustrated by the morphology of cellular substrates obtained from FEA and by optical images under 60% stretching, shown in Figure 2c,d for 40% and 80% porosities, respectively. At low porosity ( $\Phi = 40\%$ , Figure 2c), the bending stiffness ( $\approx \delta^3$ ) of the inclined cellular walls (Figure S2, Supporting Information) is sufficiently large to resist rotation around the joint. At high porosity ( $\Phi = 80\%$ , Figure 2d), these walls rotate to orientations that are almost parallel to the horizontal direction, which leads to significant dimensional reduction in the lateral direction and therefore different behaviors in the Poisson's ratio and shapes of the stress–strain curve.

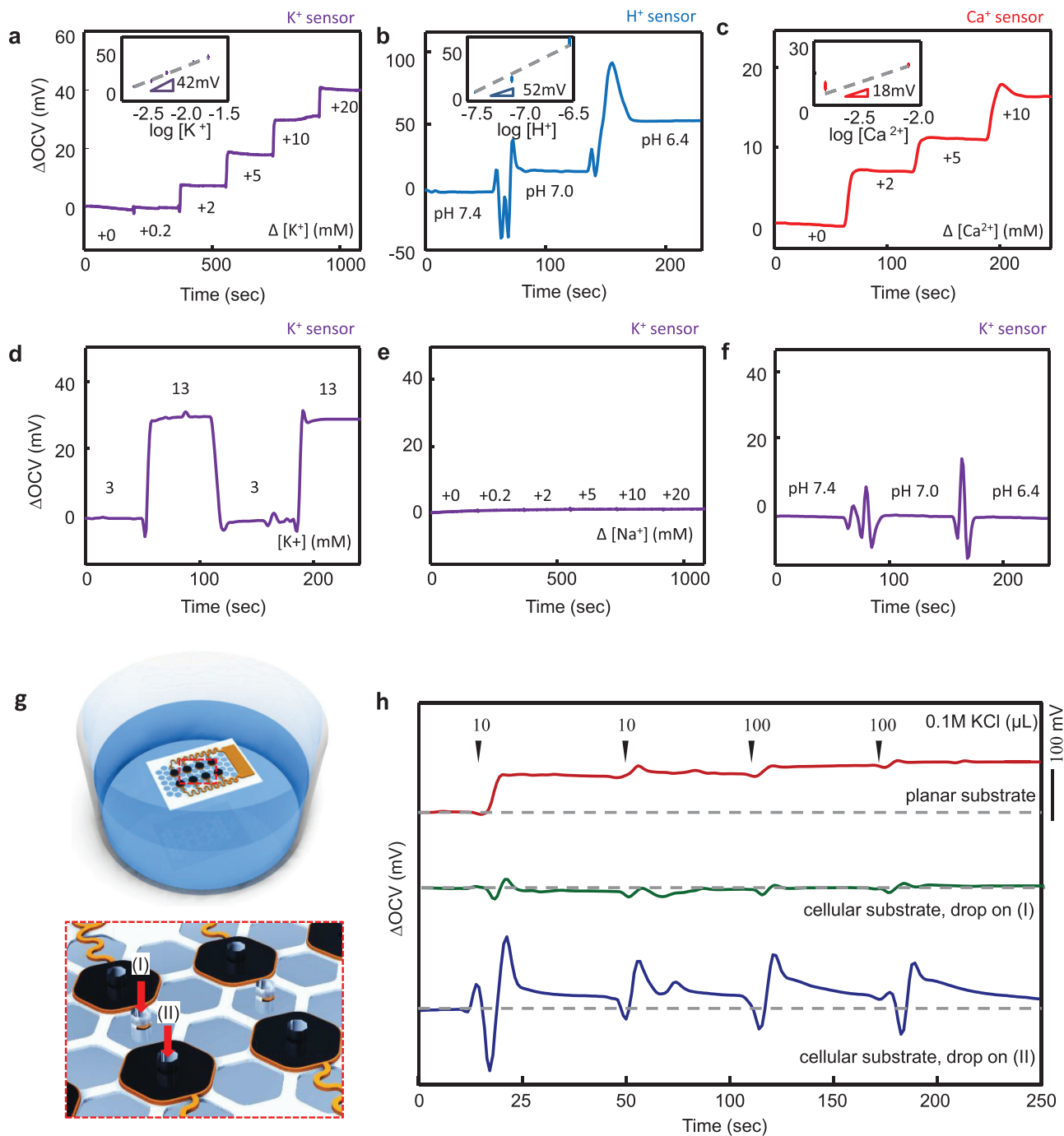
Figure 2e–h shows FEA results (Figure 2e,f) and optical images (Figure 2g,h) of the ion sensor (50  $\mu\text{m}$  PVC/1.5  $\mu\text{m}$  PI/200 nm Au/1.5  $\mu\text{m}$  PI, with the elastic modulus 1 GPa and Poisson's ratio 0.34 for PVC, 2.5 GPa and 0.34 for PI, and 80 GPa and 0.44 for Au, respectively) mounted on 300  $\mu\text{m}$  thick cellular and solid substrates (PDMS with the elastic modulus 0.5 MPa and Poisson's ratio 0.5), respectively, under 30% stretching. For both cases, the morphologies obtained by FEA agree well with the experiment. For the cellular substrate under 30% stretching (Figure 2e), the maximum strain in the Au is  $\approx 1\%$ , which is below the fracture strain, 10%.<sup>[22]</sup> For the solid substrate under the same 30% stretching (Figure 2f), the maximum strain in Au is 12%, which exceeds the fracture strain. For 0.3% yield strain for Au, the elastic stretchability of the entire system is  $\approx 12\%$  for the cellular substrate as in Figure S4a (Supporting Information), but only  $\approx 2\%$  for the solid substrate as in Figure S4b (Supporting Information). The pores in the cellular substrate do not constrain buckling of the serpentine, which leads to reduced strain in Au and therefore larger stretchability than that of the solid substrate. Figure S5 (Supporting Information) shows a modified serpentine design with a longer arm segment, which gives a much higher elastic stretchability  $\approx 28\%$  than  $\approx 12\%$ . Figure 2i gives the stress–strain curves of the cellular case with and without the ion sensor, where FEA once again agrees well with experiments. The effective moduli are  $\approx 100$  and  $\approx 50$  kPa for the cellular substrate with and without the ion sensor, respectively, which are smaller than the skin modulus ( $\approx 130$  kPa),<sup>[23]</sup> suggesting that the system will impose minimal mechanical constraints on the skin.

Figure 3 summarizes the analytical performance of ion selective electrodes in this type of construct. The tests involved immersion of sensor arrays in 100 mL of 0.1 M phosphate buffered saline (PBS) (pH 7.4,  $137 \times 10^{-3}$  M NaCl,  $2.7 \times 10^{-3}$  M KCl,  $\text{Na}_2\text{HPO}_4$   $10 \times 10^{-3}$  M,  $\text{KH}_2\text{PO}_4$   $1.8 \times 10^{-3}$  M) as a base solution. The addition of 1 M KCl, 0.1 M  $\text{CaCl}_2$ , 1 N HCl solutions by micropipette under agitation with a magnetic stirring bar introduced controlled amounts of  $\text{K}^+$ ,  $\text{Ca}^{2+}$ , and  $\text{H}^+$ , respectively. Figure 3a depicts a representative open-circuit voltage (OCV) response of a sensor of  $\text{K}^+$  ions. The numbers in the graph indicate changes in the molarity of  $\text{K}^+$  ions from the 0.1 M PBS solutions as the ions are introduced. The voltage response of the electrode results from the selective binding of ions to the ionophores embedded in the PVC membrane. Binding of positively charged ions results in potential differences across the membrane and the test solution interface.<sup>[18]</sup> The OCV of the electrodes follows this change in the membrane potential, and

increases together with the target ion concentrations in the test solution. The response time is largely independent of the magnitudes of changes in concentration, over a relevant range, with good reversibility without hysteresis. Figure 3b,c shows the results of two other types of ion sensors,  $\text{H}^+$  and  $\text{Ca}^{2+}$ . Here, the primary target cations,  $\text{K}^+$ ,  $\text{H}^+$ , and  $\text{Ca}^{2+}$  were chosen for their importance in biological systems.<sup>[24–27]</sup> The selectivity of the sensor response to  $\text{H}^+$  and  $\text{Ca}^{2+}$  results from changes in the PVC membrane, from the  $\text{K}^+$ -binding ionophore (Valinomycin; potassium ionophore I, Fluka) to tridecylamine (hydrogen ionophore I, Fluka) and ETH 1001 (calcium ionophore I, Fluka) for  $\text{H}^+$  and  $\text{Ca}^{2+}$  sensors, respectively. Figure 3b,c depicts representative results from  $\text{H}^+$  and  $\text{Ca}^{2+}$  sensors as ions are injected into the test solution. The comparatively large fluctuations observed in the case of the  $\text{H}^+$  sensor follow from the relatively low equilibrated  $\text{H}^+$  concentrations in the pH buffered solution. Phosphates were removed from the test solution for  $\text{Ca}^{2+}$  ion sensors to avoid precipitation of Ca phosphates. We performed statistical studies on 24 electrodes from 3 sensors. The data in Figure 3 are representative. The fabrication yield was  $>90\%$ . The measured values of OCV at different ion concentrations yield calibration curves, as presented in the insets of Figure 3a,b,c. The results show a linear dependence of OCV on ion concentration with slopes of 42.2, 51.8, 18.3 mV/log[ion] for the  $\text{K}^+$ ,  $\text{H}^+$ , and  $\text{Ca}^{2+}$ , respectively. The small slope for the  $\text{Ca}^{2+}$  sensor is expected from the Nernst equation due to its divalent charge.<sup>[18]</sup> The error ranges of the reported changes in the open-circuit voltages are from  $3.1 \times 10^{-1}$  to  $1.2 \times 10^0$  mV for  $\text{K}^+$  sensor,  $2.6 \times 10^0$  to  $3.3 \times 10^0$  mV for  $\text{H}^+$  sensor,  $1.3 \times 10^{-1}$  to  $1.7 \times 10^0$  mV for  $\text{Ca}^{2+}$  depending on the measuring ion concentrations. Error bars appear on the calibration curves in the insets of Figure 3a–c. *R* values for the linear fitting are 0.98, 0.96, and 0.91 for  $\text{K}^+$ ,  $\text{H}^+$ , and  $\text{Ca}^{2+}$ , respectively. The calibration range covers that for ion concentrations in extracellular fluids in most biological systems. The range includes  $3\text{--}40 \times 10^{-3}$  M,  $10^{-6.4}\text{--}10^{-7.4}$  M,  $0\text{--}10 \times 10^{-3}$  M for  $\text{K}^+$ ,  $\text{H}^+$  and  $\text{Ca}^{2+}$  in saline solutions, respectively.

Figure 3d shows reversibility of the OCV response when the  $\text{K}^+$  selective electrode is immersed in  $3 \times 10^{-3}$  and  $13 \times 10^{-3}$  M  $\text{K}^+$  PBS solutions interchangeably. The behavior indicates little or no hysteresis, as expected since the change in potential follows from a reversible chemical equilibrium associated with ion binding to the ionophore.<sup>[18]</sup> Figure 3e,h shows that the OCVs do not change upon introduction of interfering ions  $\text{Na}^+$  and  $\text{H}^+$  to the  $\text{K}^+$  selective electrode. The graph indicates that the sensors function at levels comparable to those of previously reported sensors on nonstretchable supports in terms of sensitivity, selectivity, and reversibility in the biologically relevant range of ion concentrations.<sup>[25,26,28]</sup> The sensors show a stable operation for up to 2 d of continuous immersion in aqueous solutions. Failure modes include leaching of ionophores into the surrounding solution and delamination of certain layers in the sensors. Further optimization of the materials and device designs has the potential to increase the lifetimes.

Figure 3g,h highlights capabilities in spatiotemporal mapping that follow from the use of these sensors on cellular substrates. Figure 3g shows the experimental apparatus used to create local changes in ion concentration. The setup used a 1.5 L bath of deionized water to minimize changes in ion concentration



**Figure 3.** Selective ion sensing and spatiotemporal mapping: open-circuit voltage (OCV) responses of: a) K<sup>+</sup>, b) H<sup>+</sup>, and c) Ca<sup>2+</sup> sensors in the saline solutions. The insets show the corresponding calibration curves. d) Reversibility of K<sup>+</sup> ion selective electrode. e, f) Selectivity of K<sup>+</sup> ion selective electrode against Na<sup>+</sup> (e) and H<sup>+</sup> (f). g) Schematic diagram of the experimental setup. h) Dependence of the OCV response on the substrate designs.

levels in a test solution, with the sensors fixed under a cover of PDMS (1 cm thick). Injection of 0.1 M KCl solution occurred at the open regions of the cellular substrate (Figure 3g,I) or at the electrode areas (Figure 3g,II), through holes ( $\approx 1 \text{ mm}^2$ ) in the PDMS. Figure 3h summarizes key results upon a series of injections of K<sup>+</sup>. The red line shows responses from sensors mounted on the nonporous, planar substrate. The accumulated increase in OCV corresponds to an associated accumulation of

K<sup>+</sup> between the sensor and the top PDMS. The relative changes in open-circuit potentials upon consecutive ion injection follow log scale ratios of the accumulated ion concentrations, consistent with the Nernst equation. However, the sensors on the cellular substrate exhibit a significantly different response due to changes in solution diffusion across the substrate. The green line shows the change in OCV upon injection of K<sup>+</sup> to an open, porous area of the cellular substrate (Figure 3g,I). The constant

OCV baseline indicates that  $K^+$  diffuses to the bulk water with minimal effect on the OCV of the sensor adjacent to the pore. The blue line shows the case of addition of  $K^+$  directly onto the sensor (Figure 3g,II). Here, an immediate rise in OCV corresponds to an increase in local  $K^+$  concentration at the sensor. The initial oscillatory response results from artifacts associated with injection-induced fluid flow. A subsequent increase of the potential is followed by a gradual decrease as ions diffuse into the surroundings without accumulation. The results demonstrate key advantages of the open cellular substrates in spatiotemporal mapping of a localized ion concentration over the planar alternative by enabling solution flow and diffusion.

### 3. Conclusion

The materials, designs, and integration strategies presented here provide a framework for chemical sensors capable of monitoring biomarkers in extracellular fluid, with soft physical form factors to facilitate biointegration. Fluid permeability across the sensors minimizes accumulation artifacts induced by the impermeability of conventional substrates. The envisioned advantages of this system for biological applications are in: i) capabilities for intimate and persistent contact that follows from the advanced materials' integration and their soft mechanics, ii) improved accuracy in spatiotemporal mapping of target chemicals due to facilitated flow, and iii) long-term use of the sensor without chemical/mechanical irritation on the mounted organs. As an advanced form of bioelectronic sensors, cellular design schemes can also have potential for use in other types of monitoring systems that target various types of electrophysiological signals and chemical biomarkers.

### 4. Experimental Section

**Fabrication of the Electrode:** PMMA (MicroChem, USA) coated on a 4 inch silicon wafer (University wafer, USA) served as a sacrificial layer to facilitate release. Spin casting and thermally curing (2 h at 250 °C in a vacuum oven) a film of polyimide (PI) (2  $\mu$ m in thickness, HD Microsystems, USA) yielded an overcoat on the PMMA. Photolithographic patterning of bilayers of Cr (5 nm)/Au (200 nm) deposited by electron beam evaporation (AJA International, USA) defined the conductive elements of the sensor. A second film of PI served as a top encapsulation layer. Reactive ion etching (RIE) (200 mTorr, 20 sccm  $O_2$ , 150 W for 10 min) defined open areas in the PI to define the sensing interface. Immersion in acetone for 1 h allowed retrieval of the sensor onto a water-soluble tape. Bilayers of Ti (5 nm)/ $SiO_2$  (50 nm) deposited onto the backside facilitated bonding to a UV-treated substrate of PDMS (Sylgard 184, Dow Corning, USA). Dissolving the water-soluble tape by dipping the samples into water and then drying at 70 °C prepared the systems for further processing and testing. The contact pads bonded to an anisotropic conductive film (ACF) for attachment to a printed circuit board. The back side of ACF and the contact pads were coated by PDMS to prevent the permeation of liquid into the circuit during measurement. PEDOT/PSS was electrodeposited by 15 cycles of cyclic voltammetry from -0.2 to 1 V in an aqueous bath of  $10 \times 10^{-3}$  M EDOT and 0.1 M NaPSS solution.<sup>[26]</sup> Ion selective membranes were prepared by dissolving 66 mg of 1.8% carboxylated poly(vinyl chloride) (PVC-COOH) and 131 mg bis(2-ethylhexyl)sebacate in 1.5 mL THF.<sup>[29]</sup> Ionophores (2 mg of Valinomycin (potassium ionophore I, Fluka), 2 mg of tridecylamine (hydrogen ionophore I, Fluka, USA) or 8 mg of ETH 1001 (calcium ionophore I, Fluka) was added for potassium, hydrogen,

calcium ion selective membranes, respectively. 1, 1, 3 mg of potassium tetrakis (4-chlorophenyl)borate served as a lipophilic salt for each type of ion sensors. Drop casting of 1.5  $\mu$ L of the membrane yielded the ion selective electrodes.<sup>[25]</sup> The sample was dried overnight to evaporate THF and baked at 150 °C for 10 min.<sup>[29]</sup> The sensor was conditioned in 0.1 M KCl ( $K^+$  sensor) or 0.1 M Ca analytical standard solution ( $Ca^{2+}$  sensor) or phosphate pH 7 buffer ( $H^+$  sensor) solution for more than 3 h prior to electrochemical tests. All reagents for the membrane preparation and conditioning were purchased from Sigma-Aldrich, USA.

**Fabrication of the Cellular Substrate:** PMMA (MicroChem) coated on photocurable epoxy (SU-8 2150, MicroChem) mold served as a sacrificial layer to facilitate release. Spin casting and thermally curing (2 h at 70 °C) PDMS yielded a patterned cellular substrate. Undercutting by immersing in acetone removed the PMMA layer to allow release of the PDMS for subsequent integration with the sensor arrays.

**Measurements of Open-Circuit Voltage:** A saturated Ag/AgCl electrode (BASi, USA) served as a reference electrode. 100 mL of 0.1 M PBS (pH 7.4,  $137 \times 10^{-3}$  M NaCl,  $2.7 \times 10^{-3}$  M KCl,  $Na_2HPO_4$   $10 \times 10^{-3}$  M,  $KH_2PO_4$   $1.8 \times 10^{-3}$  M) was used as a base test solution. (Phosphates were removed for  $Ca^{2+}$  test to avoid Ca phosphate precipitates.) 1 M KCl, 0.1 M  $CaCl_2$ , 1 N HCl solutions were added under agitation with a magnetic stirring bar to obtain a calibration curve. A VMP potentiostat (Biologic Technologies, France) or a GAMRY Reference 6000 potentiostat/galvanostat (GAMRY, USA) with a custom-built multiplexer was used for data acquisition.<sup>[27]</sup> The calibration range covers the typical range of ion concentration in extracellular fluids.

**Measurements of Stress-Strain Responses:** Mechanical properties of the sensors were measured with a dynamic mechanical analyzer (DMA Q800, TA instruments) under uniaxial tensile loading at room temperature.

### Supporting Information

Supporting Information is available from the Wiley Online Library or from the author.

### Acknowledgements

Y.K.L., K.-I.J., Y.M., and A.K. contributed equally to this work. Y.K.L. acknowledges the support from Kwanjeong Educational Foundation. Y.M. and X.F. acknowledge the support from the National Basic Research Program of China (Grant No. 2015CB351900) and National Natural Science Foundation of China (Grant Nos. 11402135 and 11320101001). Y.H. acknowledges the support from NSF (Grant Nos. DMR1121262, CMMI1300846, CMMI1400169, and CMMI1534120) and the NIH (Grant No. R01EB019337). K.-I.J. acknowledges the support from the DGIST Start-up Funding Program of the Ministry of Science (2016100001).

Received: October 19, 2016

Revised: November 18, 2016

Published online: January 9, 2017

- [1] D.-Y. Khang, H. Jiang, Y. Huang, J. A. Rogers, *Science* **2006**, 311, 208.
- [2] D.-H. Kim, J.-H. Ahn, W. M. Choi, H.-S. Kim, T.-H. Kim, J. Song, Y. Y. Huang, Z. Liu, C. Lu, J. A. Rogers, *Science* **2008**, 320, 507.
- [3] J. A. Rogers, T. Someya, Y. Huang, *Science* **2010**, 327, 1603.
- [4] T. Sekitani, Y. Noguchi, K. Hata, T. Fukushima, T. Aida, T. Someya, *Science* **2008**, 321, 1468.
- [5] T. Someya, Y. Kato, T. Sekitani, S. Iba, Y. Noguchi, Y. Murase, H. Kawaguchi, T. Sakurai, *Proc. Natl. Acad. Sci. USA* **2005**, 102, 12321.

- [6] S. Wagner, *MRS Bull.* **2012**, 37, 207.
- [7] I. R. Mineev, P. Musienko, A. Hirsch, Q. Barraud, N. Wenger, E. M. Moraud, J. Gandar, M. Capogrosso, T. Milekovic, L. Asboth, R. F. Torres, N. Vachicouras, Q. Liu, N. Pavlova, S. Duis, A. Larmagnac, J. Vörös, S. Micera, Z. Suo, G. Courtine, S. P. Lacour, *Science* **2015**, 347, 6218.
- [8] T. Kim, J. G. McCall, Y. H. Jung, X. Huang, E. R. Siuda, Y. Li, J. Song, Y. M. Song, H. A. Pao, R.-H. Kim, C. Lu, S. D. Lee, I.-S. Song, G. Shin, R. Al-Hasani, S. Kim, M. P. Tan, Y. Huang, F. G. Omenetto, J. A. Rogers, M. R. Bruchas, *Science* **2013**, 340, 211.
- [9] W.-H. Yeo, Y.-S. Kim, J. Lee, A. Ameen, L. Shi, M. Li, S. Wang, R. Ma, S. H. Jin, Z. Kang, Y. Huang, J. A. Rogers, *Adv. Mater.* **2013**, 25, 2773.
- [10] M. Kaltenbrunner, T. Sekitani, J. Reeder, T. Yokota, K. Kuribara, T. Tokuhara, M. Drack, R. Schwödiauer, I. Graz, S. Bauer-Gogonea, S. Bauer, T. Someya, *Nature* **2013**, 499, 458.
- [11] J.-W. Jeong, W.-H. Yeo, A. Akhtar, J. J. S. Norton, Y.-J. Kwack, S. Li, S.-Y. Jung, Y. Su, W. Lee, J. Xia, H. Cheng, Y. Huang, W.-S. Choi, T. Bretl, J. A. Rogers, *Adv. Mater.* **2013**, 25, 6839.
- [12] K.-I. Jang, S. Y. Han, S. Xu, K. E. Mathewson, Y. Zhang, J.-W. Jeong, G.-T. Kim, R. C. Webb, J. W. Lee, T. J. Dawidczyk, R. H. Kim, Y. M. Song, W.-H. Yeo, S. Kim, H. Cheng, S. Il Rhee, J. Chung, B. Kim, H. U. Chung, D. Lee, Y. Yang, M. Cho, J. G. Gaspar, R. Carbonari, M. Fabiani, G. Gratton, Y. Huang, J. A. Rogers, *Nat. Commun.* **2014**, 5, 4779.
- [13] K.-I. Jang, H. N. Jung, J. W. Lee, S. Xu, Y. H. Liu, Y. Ma, J.-W. Jeong, Y. M. Song, J. Kim, B. H. Kim, A. Banks, J. W. Kwak, Y. Yang, D. Shi, Z. Wei, X. Feng, U. Paik, Y. Huang, R. Ghaffari, J. A. Rogers, *Adv. Funct. Mater.* **2016**, 26, 7281.
- [14] R. Maskeliunas, R. Damasevicius, I. Martisius, M. Vasiljevas, *PeerJ* **2016**, 4, 1746.
- [15] W. Gao, S. Emaminejad, H. Y. Y. Nyein, S. Challa, K. Chen, A. Peck, H. M. Fahad, H. Ota, H. Shiraki, D. Kiriya, D.-H. Lien, G. A. Brooks, R. W. Davis, A. Javey, *Nature* **2016**, 529, 509.
- [16] A. J. Bandodkar, J. Wang, *Trends Biotechnol.* **2014**, 32, 363.
- [17] J. Bobacka, *Electroanalysis* **2006**, 18, 7.
- [18] E. Bakker, P. Bühlmann, E. Pretsch, *Chem. Rev.* **1997**, 97, 3083.
- [19] ANSYS FLUENT User's Guide, V14.5, **2015**.
- [20] E. Samson, J. Marchand, K. A. Snyder, *Mater. Struct.* **2003**, 36, 156.
- [21] ABAQUS Analysis User's Manual, V6.10, **2010**.
- [22] H. Hocheng, C.-M. Chen, *Sensors* **2014**, 14, 11855.
- [23] C. H. Lee, Y. Ma, K.-I. Jang, A. Banks, T. Pan, X. Feng, J. S. Kim, D. Kang, M. S. Raj, B. L. McGrane, B. Morey, X. Wang, R. Ghaffari, Y. Huang, J. A. Rogers, *Adv. Funct. Mater.* **2015**, 25, 3698.
- [24] R. P. RUBIN, *Pharmacol. Rev.* **1970**, 22, 389.
- [25] V. V. Cosofret, M. Erdosy, T. A. Johnson, R. P. Buck, R. B. Ash, M. R. Neuman, *Anal. Chem.* **1995**, 67, 1647.
- [26] M. Odijk, E. J. van der Wouden, W. Olthuis, M. D. Ferrari, E. A. Tolner, A. M. J. M. van den Maagdenberg, A. van den Berg, *Sens. Actuators, B Chem.* **2015**, 207, 945.
- [27] H.-J. Chung, M. S. Sulkin, J.-S. Kim, C. Goudeseune, H.-Y. Chao, J. W. Song, S. Y. Yang, Y.-Y. Hsu, R. Ghaffari, I. R. Efimov, J. A. Rogers, *Adv. Healthcare Mater.* **2014**, 3, 59.
- [28] A. J. Bandodkar, D. Molinnus, O. Mirza, T. Guinovart, J. R. Windmiller, G. Valdés-Ramírez, F. J. Andrade, M. J. Schöning, J. Wang, *Biosens. Bioelectron.* **2014**, 54, 603.
- [29] E. Lindner, V. V. Cosofret, S. Ufer, R. P. Buck, R. P. Kusy, R. B. Ash, H. T. Nagle, *J. Chem. Soc. Faraday Trans.* **1993**, 89, 361.